The structural modulation of amorphous 2D tungsten oxide materials in magnetron sputtering

Bo Zhang[a], Veronika Cicmancova[b], Benes Ludvik[b], Stanislav Slang[b], Petr Kutalek[c], Martin Motola [d], Tomas Wagner[b,e]

[a]College of Physics, Hebei Normal University, Shijiazhuang 050024, China

[b]Center of Materials and Nanotechnologies, Faculty of Chemical Technology, University of Pardubice, Nam. Cs. Legii 565, 530 02 Pardubice, Czech Republic

[c]Joint Laboratory of Solid State Chemistry, University of Pardubice, Studentska 84, 532 10 Pardubice, Czech Republic

[d]Department of Inorganic Chemistry, Faculty of Natural Sciences, Comenius University in Bratislava, Ilkovicova 6 – Mlynska dolina, 842 15, Bratislava, Slovak Republic

[e]Department of General and Inorganic Chemistry, Faculty of Chemical Technology, University of Pardubice, Studentska 573, 532 10 Pardubice, Czech Republic

KEYWORDS magnetron sputtering, 2D material

ABSTRACT

2D oxide materials have gained tremendous attention in the applications. Herein, we report a synthesis route of 2D WO_3 materials via magnetron sputtering. A deposition between 2D monolayers and thin film structure are accomplished according to the temperature of substrate. And 2D monolayers are only formed on a cooled substrate. Ag doping helps to exfoliate 2D WO_3 into freestanding monolayers,

in which the thickness of 2D monolayer is only ~3nm. The ultra large size of 2D WO_3 shows unique features from the traditional 2D material. Resistive switching device and photocatalysis are discussed as examples of application. There is a clear intermediate resistance state in the device with 2D structure. And the failure of resistive switching device is closely related with the 2D structure of WO_3. In the application of photocatalysis, we utilize an improved the two-step exfoliation, achieving a stack of WO_3 monolayers with a large internal volume. The enhancements of photocatalysis are obtained with 2D WO_3 after exfoliation.

INTRODUCTION

The large surface to volume ratio of nanostructured material has been published for many potential applications.[1-4] Therefore, many different nanostructures have been found, including nanowire, nanoflakes and nanoparticles. [5-9] Among all nano structure oxides, two-dimensional oxide materials have attracted tremendous attention in the past few years, and various synthesis routes have been published.[10] The layered transition metal oxides, with interlayer spacing, have been exfoliated with a cation exchange-assistant liquid treatment.[11] Optionally, the intercalated layer can be further exfoliated into nanosheets by the help of sonication and or shear factors. The advantages of these exfoliation methods show a high yield and up-scaling possibilities. However, the oxides exfoliated in these methods must be layered, which restricts its application. [12] Therefore, as an alternative route, many 2D metal oxides are synthesized from the oxidation of non-oxidic materials.[13] For instance, 2D sheets of CuO/Cu_2O have been prepared from the oxidation of Cu surface.[14] And our group also successfully prepared 2D WO_3 sheets in the similar way.[15] Nevertheless, the oxidation of metal is not easy to be precisely manipulated. Except for the methods discussed above, a chemical reaction related vapor depositions, including CVD (Chemical Vapor Deposition) and ALD (Atomic Layer Deposition), are promising for the synthesis of various 2D oxides.[16] However, ALD and CVD methods are restricted by the high cost of instrument. Moreover, the synthesis processes have to be precisely regulated, including precursor, substrate, catalysts, temperature, and gas flow rate.[17] Although many synthesis routes have been developed as discussed above, there is still a need to search for a low cost and easily accessible method.

2D nanosheet of WO_3 has been applied in the field of NO_2, H_2 gas-sensing and UV photo detector.[18,19] Furthermore, WO_3/TiO_2 heterojunction has been widely studied in super capacitance.[16] The versatile synthesis of 2D WO_3 has been described in literature.[20] In general, chemical wet routes are more popular to synthesis 2D WO_3 in the recent years, due to low lost and efficiency.[21] It is commonly initiated from tungsten compounds, for instance sodium tungstate dehydrate.[20] The final WO_3 products are often in powder form.[22] ALD has also been developed to prepare 2D WO_3 in recent years. [23,24] Besides these methods, a new method, refereed as solid-liquid phase arc discharge, has been utilized for synthesis of 2D WO_3 nanosheets.[25] The thickness of WO_3 monolayer is in the range of 4-5nm.

In our previous study, we have prepared a series of layered materials based on magnetron sputtering and thermal evaporation, including chalcogenides and metals.[26-27] In this paper, we develops a new method to synthesize 2D WO_3 material and it depends simply on a commercial magnetron sputtering instrument in a normal condition. The structure of 2D WO_3 is amorphous and the thickness of freestanding monolayer is less than 3nm. We further modify the structure of WO_3 between 2D and thin film via the condition of magnetron sputtering. In the RRAM (Resistive random-access memory) device, 2D WO_3 material clearly influences the behavior of resistive switching loop. In the application of photocatalysis, 2D WO_3 shows a better performance than the thin film WO_3.

EXPERIMENT

The formation of 2D material were studied in the first part of the paper. During the deposition of WO_3, the substrates were maintained in a cooled state or a normal state. In order to perform a substrate cooling, a stainless holder equipped with a mask was fabricated, as shown in Figure S1. Before deposition, wafers were cut into the size of 0.8cm × 0.8cm and bonded to a stainless steel holder directly via a thermal conducive tape (thermal conductivity 1.5w/(m·k)). The thermal conductive tape helps to transfer the heat (generated during sputtering) from substrate to a stainless-steel holder. Differently, the silicon wafer substrate without cooling was attached to a silica glass, as shown in Figure S2. Due to low thermal conductivity of silica glass, the thermal transfer is restricted. WO_3 was

sputtered on cooled substrate and normal substrate (Refereed as **CS** and **NS**) at 3.35W/cm^2 in a pure argon environment with 1.5Pa for 1hour.

The exfoliation was proceeded by the precipitation of Ag nanoparticles. Firstly, a layer of Ag (100nm) was evaporated onto two sets of samples (CS, NS). The heat from the Ag vapour gives enough energy for a diffusion of Ag ions into the interior of WO_3. Due to the saturation of Ag, Ag particles appear to delaminate the adjacent of WO_3 monolayers. Secondly, the iron chloride was used to remove the extra residue of Ag thin film on the topmost of WO_3. The morphology and structure of samples were characterized via High Resolution Transmission Electron Microscope (HRTEM, Olympus BX51), Scanning Electron Microscopy (SEM, JEOL 7500), Atomic Force Microscope (AFM, AFM Solver Pro M) and nanointendation (bruker ti980, berkovich intender). And the steady-state thermal stress was analyzed by the Ansys software. XPS (X-ray Photoemission Spectroscopy) experiments were performed in a ThermoFisher Scientific K-alpha system equipped with a monochromatic AlKα X-ray radiation (1486.6eV) in ultrahigh vacuum conditions (base pressure 5×10^{-10}Pa). Survey scans were performed at constant pass energy (50eV) and high-resolution measurements at 0.05eV.

In the second part of the paper, the resistive switching device was fabricated in cross-bar configuration，in which the bottom and top electrodes were tungsten and silver, respectively. The contact area of electrodes was 0.1mm×0.1mm. The WO_3 layer was sputtered with 3.35W/cm^2 in a pure argon environment with 1.5Pa for 1hour, onto two sets of substrates (NS, CS). The cycling of DC sweep was carried on via Keithley 2600, equipped with tungsten coated probe.

In the third part of the paper, WO_3 (used for photocatalysis) was processed with slightly different steps. Firstly, WO_3(NS) was deposited onto silicon wafer via RF magnetron sputtering at 3.45W/cm^2 power density and 0.5Pa argon pressure for an hour. The high density of power and low argon pressure result in a good adhesion between WO_3 and substrate. Secondly, WO_3 was then annealed at 160℃ for 1h. This step helps to exfoliate the material. Afterwards, 20nm Ag layer was deposited by thermal evaporation at 0.1nm/s. During deposition, the Ag diffuses into WO_3 layer. And thinner Ag layer facilitates the etching step. In order to expose the WO_3 layer, the top Ag layer was etched with the

6.3g/l $FeCl_3$ acetone solution, in which Ag layer is reacted into AgCl compound. At last, the compound was further rinsed and cleaned with distilled water. For the liquid phase photocatalysis, the photocatalytic degradation activities of all samples were evaluated using photodegradation of methylene blue solution (MB, initial concentration 1×10^{-5} M). The samples were irradiated by a LED-based UV lamp (10 W, λ=365nm ± 5 nm), and the absorbance of the MB solution was measured (10 or 30min steps) by a UV-VIS spectrometer (S-200, Boeco) at a wavelength of 670 nm to monitor the degradation rates. The Raman spectra were measured by themo scientific DXR2 with laser power 25mW and 2μm laser spot.

RESULT AND DISCUSSION

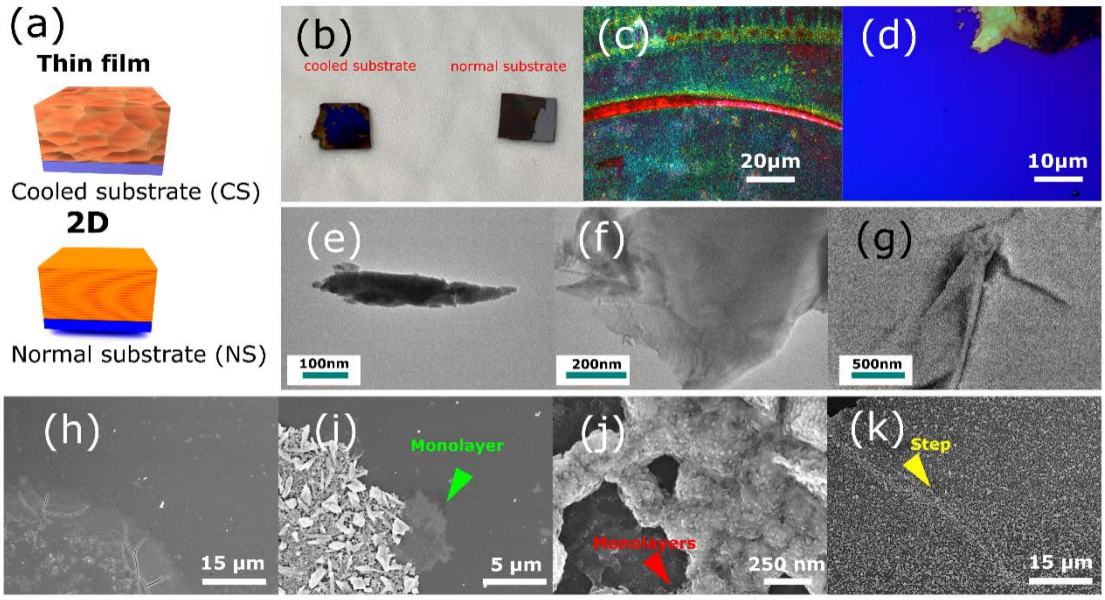

Figure 1. a) The graphic illustration of thin film and 2D structures. b) The photo of WO_3(CS, NS) samples. c) The optical microscopic image of WO_3(NS) after Ag doping-etching. d) The optical microscopic image of WO_3(CS) after Ag doping-etching. e) TEM images of WO_3(CS) flakes. f-g) TEM images of freestanding WO_3(NS) monolayers. h-i) The SEM images of WO_3(CS), after Ag doping-etching. j-k) The SEM images of WO_3(NS), after Ag doping-etching.

In the published papers,[15,26] we have reported a novel method for synthesis of 2D materials. However, the mechanism for the formation of monolayers was not discussed deeply in these papers. In our opinion, it is related with the stress and thermal expansion of substrate. During the process of magnetron sputtering, the temperature of substrate stays in 50-200℃.[28] Therefore, the thermal expansion between substrate and deposited material cannot be neglected. The formation of monolayers is closely related with the thermal stress and strain, which is originated from the mismatch of thermal expansion coefficients between substrate and deposited material. Hence, the stress related defects are created.[29] Furthermore, the defects develop into macro cracks in parallel with the silicon substrate, resulting in a formation of 2D monolayers. In order to study this hypothetical explanation, two devices were designed in this paper. In the first one, silicon substrate is glued to a stainless steel holder for cooling via a thermal conductive tape **(Refered as CS**) and another one is attached to a normal silica glass （**Referred as NS**). The experimental detail is shown in Figure S1 and S2. During the sputtering, the heat can transfer from the silicon substrate to the underlying stainless-steel holder constantly via thermal conductive tape in the first one experiment setup. Since the stainless steel possesses a large size and good heat conductivity, the temperature of silicon wafer maintained stable throughout the deposition. In the second one, we clamped the silicon substrate (0.8cm × 0.8cm) onto a silica glass, and the silica glass was fixed onto the stainless-steel holder. The silica glass restricts the heat transfer. Therefore, the temperature of the silicon wafer increased to 100℃ throughout sputtering. As shown in Figure 1a, the structures of WO_3 (CS and NS) are presented in a compact thin film and 2D stack of monolayers, respectively.

As a novel 2D material, we utilized an excessive Ag doping for exfoliation in our previous work. [26] Since the mismatch of thermal expansion coefficient has led to a creation of stress, the stress further creates defects and micro-voids. In our opinion, the defects or voids are distributed in parallel with the silicon substrate. Therefore, Ag particles can precipitate in the place of micro voids and separate a pair of adjacent monolayers. To this end, a thick (100 nm) Ag layer was evaporated onto the WO_3 material. Meanwhile, excessive Ag diffuses into WO_3, which is driven by the heat generated in thermal evaporation. Afterwards, the Ag residue was removed by $FeCl_3$/acetone mixed solution. In the

etching process, Ag layer and precipitated nanoparticles are transformed into AgCl in the first step and the vaporization of acetone further helps to exfoliate the adjacent monolayers. In the etching process, parts of WO_3 are disrupted. Figure 1b shows the photo of sample after etching. For the WO_3(CS), the Ag layer in combination with WO_3 monolayers are removed and a large area of silicon wafer are exposed. However, the appearance of WO_3 (NS) are not changed after Ag deposition and etching process. Therefore, the intact of WO_3 (NS) suggests that it does not have a structure of 2D monolayers. Figure 1c shows a clear step morphology at the edge of monolayer after etching. Furthermore, the image presents a red belt in the middle. The red belt might be formed, due to the light interference between monolayers. In Figure 1d, the appearance of WO_3(CS) maintains a uniform blue color before and after Ag etching. And a remaining part of Ag thin film is presented at the top side. This result is in consistent with the conclusion from Figure 1b, which WO_3(CS) is in a structure without monolayers.

The freestanding flakes for TEM were scratched from as-deposited WO_3(CS, NS) and dispersed into ethanol solution, then transformed onto the copper grid. Figure 1e-g are TEM images of WO_3(CS and NS). In Figure 1e, the flake of WO_3(CS) is in opaque without a monolayer structure. Nevertheless, the appearance of WO_3(NS) flakes is completely different from that of WO_3(CS). As shown in Figure 1f, most of flakes are observed as freestanding monolayer or folded monolayers. Those semitransparent monolayers present a low contrast image to be pinpointed. For instance, we found a large piece of WO_3(NS) monolayer only from the cracks in Figure 1g.

The SEM image of WO_3(CS) after Ag doping-etching shows a smooth and low contrast surface as shown in Figure 1h. Nevertheless, the SEM images of WO_3 (NS) (Figure 1i-k) exhibits a completely different morphology. As shown in Figure 1j, WO_3 (NS) is covered by needle like particles. And further EDS measurements (Figure S3a) conform that the needle like particles mainly contains AgCl compound. The particles are preserved on the WO_3 monolayers. The mechanism of exfoliation is explained in the following text. Initially, Ag diffuses from the Ag thin film into the underlying WO_3 monolayers. Then Ag particles are precipitated due to the saturated Ag concentration. In addition, we can see the bottom WO_3 monolayer is not covered with the needle like particles, which suggests Ag particles are not formed at the surface of bottom monolayer. There is another issue regarding with Ag

doping. Since the WO_3 stack comprises multiple monolayers, Ag ions must have certain channel to diffuse across the adjacent monolayers. To this end, we put forward a 'bridge' structure as 'Ag channels'. The SEM image in Figure 1j was taken from a partly etched region where most of WO_3 monolayers were removed. The edge of monolayers is marked with red arrow. We believe the remaining parts might serve as the 'bridge' for the migration of Ag ions, as shown in Figure S3b. Since our 2D material model consists of a 'bridge' structure, it is clearly different from the other reported 2D materials [30].

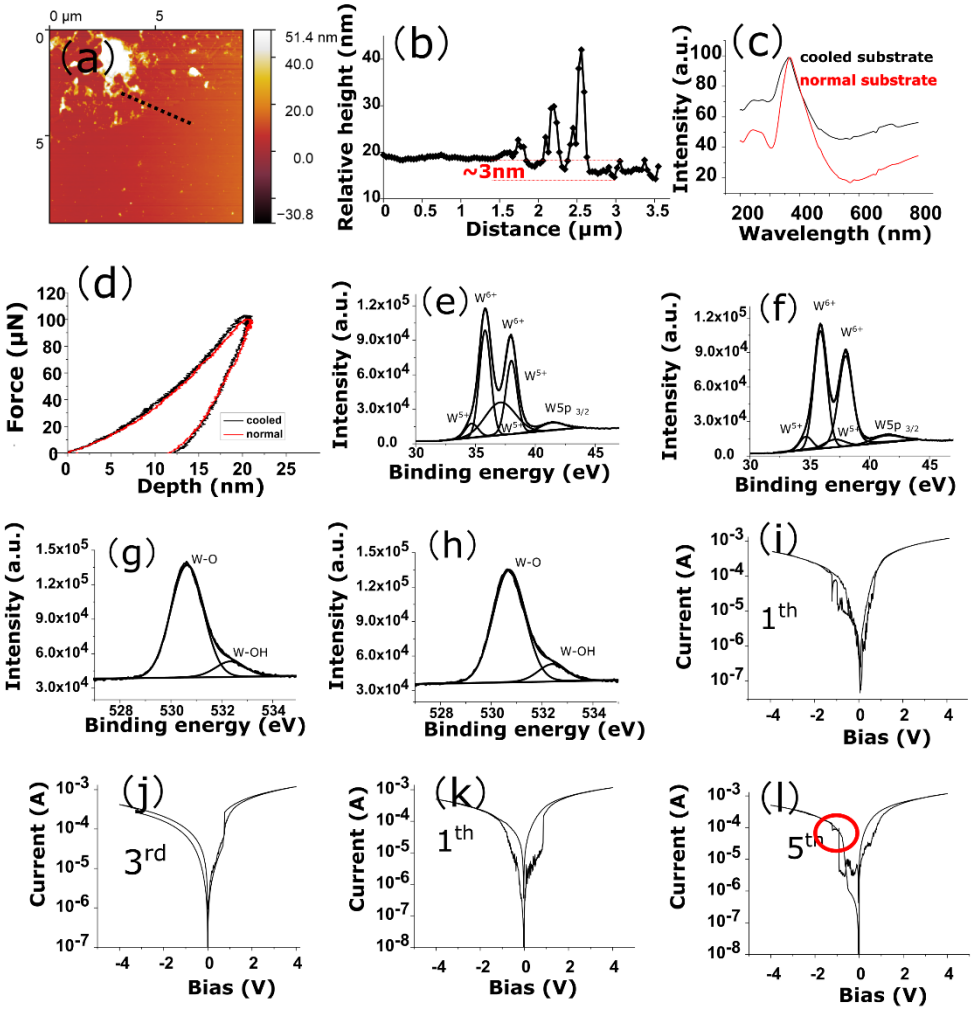

Figure 2. a) The AFM images of WO_3(CS) after removal of topmost Ag thin film. b) The profile obtained from the line in a and the height of step is marked as 3nm. c) The reflectance spectrum of WO_3(CS, NS). d) The nanoindentation of WO_3(CS, NS). e-f) The W4f spectrum of WO_3(CS, NS). g-h) O1s spectrum of WO_3(CS, NS). i-j) The resistive switching behavior of device (first and third cycles)

with the Ag/WO_3(CS)/W. k-l) The resistive switching behavior of device (first and fifth cycles) with Ag/WO_3(NS)/W.

As shown in Figure 2a and b, the height (3nm) of the step is determined by the AFM measurement. However, it might involve an air gap and AgCl particles, which the real thickness of monolayer should be less than 3nm. The UV-Vis spectra of reflectance are analysed in the range of 200-800nm wavelength, as shown in Figure 2c. One can see 2D WO_3 (NS) absorbs more light. The phenomena might be related with the scattering and interference of monolayers. Therefore, 2D WO_3 (NS) is a potential candidate for photo-catalysis. As discussed in Figure 1c and d, one could have a conclusion that WO_3(CS) is much more rigid. Therefore, another nanoindentation test was preformed for both samples, as shown in Figure 2d. And the hardness of WO_3(CS) (0.252Gpa) is slightly higher than that of WO_3(NS)(0.244Gpa), which are much smaller in comparison with the literature.[31] This phenomenon is mainly caused by our preparation method. WO_3 ceramic target was sputtered with a low power. The advantage of low power helps to protect the fragile target from broken up. As the result of that, the deposition speed is redistricted to 1.3nm/min. In the literature,[32] a reactive sputtering of metallic tungsten target in oxygen environment is more often used in deposition of WO_3, which the deposition speed and hardness of thin film are much higher.

As discussed above, 2D monolayers are possibly formed due to strain and stress. Nevertheless, it is difficult to measure the strain and stress experimentally. To this end, a finite element analysis was preformed via Ansys software. The temperature data, necessary for finite element, was collected by a thermal sensitive paper. And the mechanical property of WO_3 thin film was obtained from the nanoindentation test. The result is shown in Figure S4a. Interestingly, the stress and strain are concentrated at the edge of silicon wafer, especially at the corner. In the experiment, most of exfoliation initiates from the same region on the edge and corner, which conforms the relationship of monolayers and stress.

The chemical valence states of tungsten and oxide in the WO_3 were investigated using XPS measurements, as shown in Figure 2e-h. The XPS survey spectrums are presented in Figure S4b. The

spectra were deconvoluted with a mixed Gaussian-Lorentzian peak shape and the Shirely background subtraction was applied. The high resolution W4f spectrum is shown as a doublet of $W4f_{7/2}$ and $W4f_{5/2}$ for W valence state. Although the WO_3 was sputtered via WO_3 ceramic target in a pure argon environment, a deviation of stoichiometric ratio is expected in as-deposited material. By comparison of Figure 2e and f, one can notice the quantitation of W^{5+} state is obviously higher in WO_3(NS) sample. The temperature of substrate in normal state reached up to 100°C during deposition. The high temperature accelerates oxidation of tungsten element with the surface absorbed oxygen. The O1s spectrum is fitted with 2 peaks which represent the lattice oxygen and absorbed hydroxyl radicals in Figure 2g-h. Basically, there is no giant difference of composition between WO_3(NS) and WO_3(CS). As the result of that, the appearance differences between Figure 1c and d are not caused by the variation of composition.

Ag doped 2D WO_3(NS) is a feasible material for developing new resistive switching devices. Owing to the layered structure of 2D WO_3(NS), multilevel resistances in SET and RESET process are expected in comparison with a uniform WO_3(CS) thin film. We fabricate two devices with WO_3: Ag/WO_3 (CS)/W and Ag/WO_3 (NS)/W, which Ag and W serve as positive and negative electrodes, respectively. The DC sweep was measured with the Keithley 2612 with the step of 10mV. Figure 2 i-l show the I-V curves for both WO_3(NS, CS) in logarithm scale. In the first cycle, the both devices show a regular SET and RESET process. In the 3^{rd} and 5^{th} cycle, devices of WO_3(CS, NS) start to stop functioning properly in the RESET process. The generation of Joule heat in low resistive state attributes for the failure of devices, since we did not perform a current compliance on the working devices. A clear current step (Figure 2l, marked by the red circle) indicates a relationship between the failure of device and the monolayers. During the cycling of devices, Joule heat might exfoliate a part of the 2D WO_3, preventing the creation and dissolution of filament. Furthermore, the high resistance and low resistance state are stable in 2D WO_3 based RRAM cell after a long-term stability test, as shown in Figure S4c. In summary, the 2D structure WO_3 (NS) shows a future possibility to improve the storage density. However, there are still issues remaining unclear, for instance how the monolayer

influences the formation of conductive filament. A detailed study with different 2D oxides should be conducted in the future.

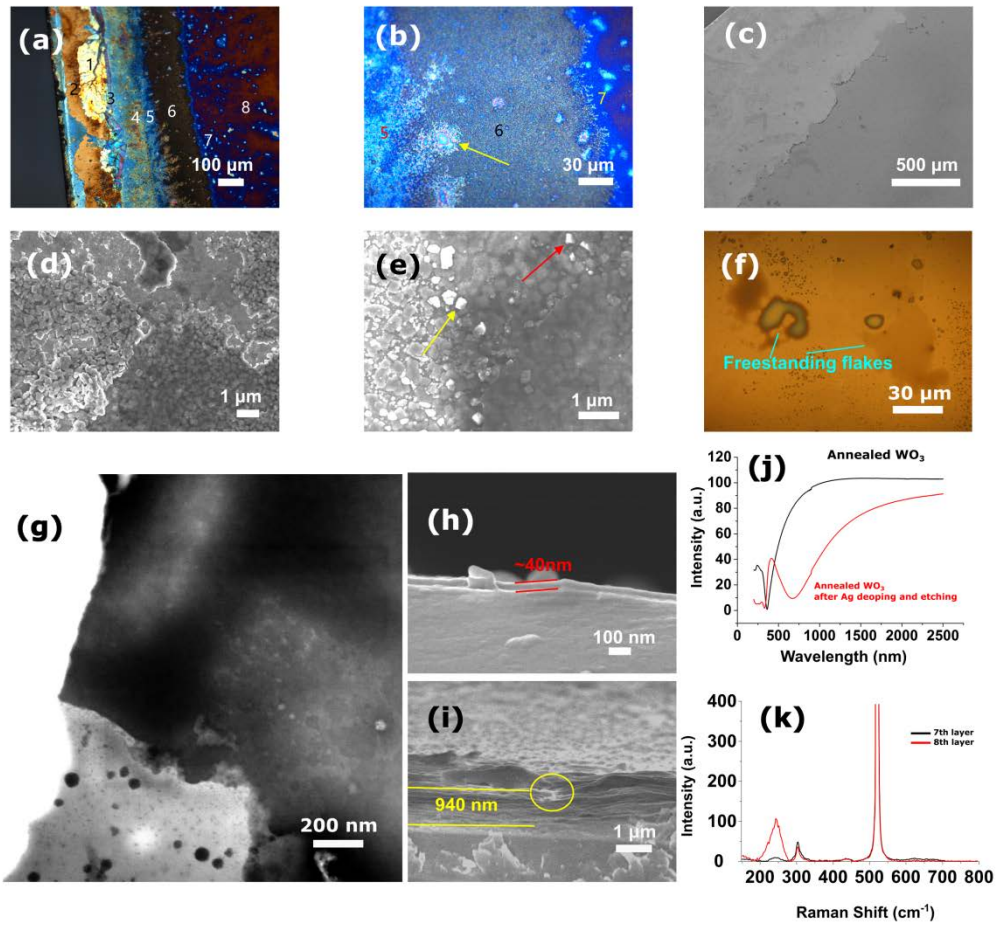

Figure 3. a) The top view of annealed WO_3 after Ag doping-etching under optical microscope, in which the layers from the top to the bottom are marked form 1-8. b) The enlarged image of a, where 5^{th} layer is marked by the arrow. c-e) SEM image of the top view in the same region of a. f) The optical microscopic image of freestanding flakes which were exfoliated from annealed WO_3 after Ag doping-etching. g) The TEM image of freestanding flakes which were exfoliated from annealed WO_3 after Ag doping-etching. h-i) The cross-sectional view of annealed WO_3 before and after Ag doping-

etching. j) The reflectance of WO_3 before and after Ag doping-etching. k) The micro Raman spectra of the 7^{th} and 8^{th} monolayer from a.

There are a few issues with the WO_3(NS). Firstly, the materials are seriously collapsed after Ag etching, as shown in Figure 1b. Secondly, the exfoliation is less efficient. One might notice the only one monolayer is exfoliated, and the rest of monolayers are still bonded firmly together in Figure 1c. It suggests the Ag doping and precipitation are still difficult to exfoliate the 2D WO_3 material. In the future applications, we may hope the sample is still bonded to the substrate after Ag etching. In Figure 3, the improvements of deposition and exfoliation were applied to the 2D WO_3 material, which made it possible for the application in photo-catalysis. The first modification was to lower argon pressure. This modification further reduces sputtering rate and the thermal expansion of substrate. The low sputtering rate improves the adhesion between 2D WO_3 and silicon substrate. Secondly, we annealed the 2D WO_3 material at 160℃ for one hour. This process has been utilized in our previous work, referred as thermal exfoliation.[15] At last, the Ag layer was controlled in a thickness of 20 nm. Thinner Ag layer facilitates the etching process.

Figure 3a shows the surface morphology of annealed WO_3, after Ag doping and etching. 8 colorful monolayers are presented. And all monolayers are bonded in a stack. Figure 3b shows an enlarged image of Figure 3a, where the edge of 5^{th} layer is marked by the yellow arrow. The SEM image (Figure 3c) at low magnification is in a low contrast, and one cannot even see the step morphology. The monolayers under high magnification (Figure 3d-e, marked by arrows) are semitransparent and particles separate the adjacent monolayers. From the EDX and XRD results (Figure S5-S6), the composition of particles is confirmed as AgCl, which is the reactive product between $FeCl_3$ and Ag particles. Figure 3f shows the freestanding WO_3 flakes on a silicon wafer, in which the color of flakes is possibly resulted from the interference.

TEM images of annealed WO_3 after doping-etching is presented in Figure 3g. After Ag thin film was etched, it is inevitable that some parts of monolayers were dispersed into the solution. The flakes were then transferred onto copper grid for TEM imaging. These opaque particles in Figure 3g are mainly

Ag particles and AgCl compound. With the increasing number of monolayers, the material transforms to opaque. The cross-sectional SEM images in Figure 3h and j show a volume expansion of Ag doped WO_3 stack after etching. As presented in Figure 3h, the original WO_3 thin film is only 40nm thick without exfoliation. After deposition of Ag layer, the Ag particles exfoliate the monolayers. We can see the thickness of stack increases to 940nm, as shown in Figure 3h-i. The 'bridge' between monolayers is shown in the yellow circle in Figure 3i). It connects the monolayers and offers channels for Ag diffusion, as shown in Figure S7.

From the UV-Vis reflectance spectra in Figure 3j, the annealed WO_3 sample after Ag doping-etching absorbs more incident light in the range of UV， which manifests a potential application for photo-catalysis. The micro-Raman spectra are shown in Figure 3k, where two spectra were measured from 7^{th} and 8^{th} monolayer of Figure 3a after Ag doping-etching. And the peak intensity at $243cm^{-1}$ from 8^{th} monolayer is clearly stronger than that of 7^{th} monolayer. The strongest peak at $520cm^{-1}$ comes from the silicon wafer, which is refereed as Si-Si LO peak.[33] The peaks at $243cm^{-1}$ and $303cm^{-1}$ represent δ(O-W-O) and γ(WO_3) vibrational modes in Ag doped WO_3 thin layer sample.[34,35]

As discussed above, the specific surface area of WO_3(NS) after annealing and Ag doping-etching treatment is greatly enhanced. The large specific area is ideal for the application in photocatalysis. Figure S8 shows photo-catalytic decomposition profile of Methylene Blue (MB), which the kinetic fitting of the curve with the respect to irradiation time. The first-order decomposition kinetics was fitted: $\ln(c/c_0) = kt$, where c_0 and c are the concentration of MB at the beginning and after the time t, and k is the pseudo-first rate kinetic constant. The photocatalytic decomposition rate of MB in delaminated Ag doped WO_3 stack is obviously stronger than the annealed compact WO_3 without Ag doping-etching. Therefore, Ag doping is essential for the exfoliation and delamination of WO_3. The amorphous solids own rich defective sites, hence pinned the Fermi level. Under the illumination of light, the electrons are transferred from the valence band (VB) or defective sites to the conduction band (CB). Meanwhile, it helps to generate hydroxyl radicals (·OH), which is responsible for the degradation of MB. In summary, we believe the enhancement of photocatalysis is partially due to the

large surface and internal area, which is similar as the other nano materials, for instance TiO_2 nanotube.[36]

CONCLUSION

In this paper, we systematically studied a novel 2D WO_3 material in the aspect of mechanism, property and applications. A modulation between thin film and 2D materials are achieved via controlling of substrate temperature. Without the cooling, the temperature of silicon wafer increases and the mismatch of silicon wafer and WO_3 results in a buildup of stress. Such stress creates the defects or micro voids in parallel direction with the silicon wafer. After doping with Ag, Ag particles precipitate in the place of voids. Therefore, Ag doped WO_3 layer is exfoliated into a stack of layers. The thickness of freestanding monolayer is thinner than 3nm, and the lateral size can be in the range of micrometers. Nevertheless, the monolayers are not presented on the cooled substrate. Therefore, the physical and chemical properties are different. Afterwards, a comparison study of RRAM devices are made between the thin film and 2D structural WO_3. And 2D monolayers is found to be related with the failure of devices. The second application of 2D WO_3 is photo-catalysis. An improved two-step exfoliation is adapted in order to have a large specific volume. The result shows an enhanced performance of annealed WO_3 after Ag doping and etching.

As magnetron sputtering method is long history PVD method with low cost and easy accessibility, our new synthesis approach for 2D WO_3 offers a future possibility for micro-electric devices and other applications. More importantly, the similar approach has been achieved for metals and chalcogenide materials. A universal synthesis method could facilitate the development of 2D materials.

REFERENCE

[1] C. L. McBean, L. Wang, D. Moronta, A. Scida, L. Li, E. S. Takeuchi, K. J. Takeuchi, A. C. Marschilok, S. S. Wong, *ACS Applied Energy Materials* **2019**, *2*, 4801.

[2] S. Ma, Y.-K. Jung, J. Ahn, J. Kyhm, J. Tan, H. Lee, G. Jang, C. U. Lee, A. Walsh, J. Moon, *Nature Communications* **2022**, *13*, 3259.

[3] W. Li, L. Hu, J. Ma, C. Jiang, S. Zhang, Y. Chen, J. Hu, X. Liu, T. Wu, D. Li, *ACS Photonics* **2022**, *9*, 2008.

[4] J. Zhang, X. L. Wang, X. H. Xia, C. D. Gu, Z. J. Zhao, J. P. Tu, *Electrochimica Acta* **2010**, *55*, 6953.

[5] J. Thangala, S. Vaddiraju, R. Bogale, R. Thurman, T. Powers, B. Deb, M. K. Sunkara, *Small* **2007**, *3*, 890.

[6] S. J. Hong, H. Jun, P. H. Borse, J. S. Lee, *International Journal of Hydrogen Energy* **2009**, *34*, 3234.

[7] H. Zhou, J. Guo, C. Wang, X. Liu, S. Shi, J. Wei, X. Pu, W. Li, D. Zhang, J. Wang, X. Ren, H. Ma, X. Shao, X. Wei, J. Zhao, J. Yin, X. Zhang, *Advanced Materials Interfaces* **2019**, *6*, 1801657.

[8] H. Li, J. Huang, Y. Shi, L. Li, *Advanced Materials Interfaces* **2019**, *6*, 1900220.

[9] T. Dong, J. Simões, Z. Yang, *Advanced Materials Interfaces* **2020**, *7*, 1901657.

[10] P. Kumbhakar, C. Chowde Gowda, P. L. Mahapatra, M. Mukherjee, K. D. Malviya, M. Chaker, A. Chandra, B. Lahiri, P. M. Ajayan, D. Jariwala, A. Singh, C. S. Tiwary, *Materials Today* **2021**, *45*, 142.

[11] I. Moriguchi, Y. Tsujigo, Y. Teraoka, S. Kagawa, *Advanced Materials* **1999**, *11*, 997.

[12] W. Liu, R. Yin, W. Shi, X. Xu, X. Shen, Q. Yin, L. Xu, X. Cao, *ACS Applied Energy Materials* **2019**, *2*, 579.

[13] J. Rooze, E. v. Rebrov, J. C. Schouten, J. T. F. Keurentjes, *Ultrasonics Sonochemistry* **2013**, *20*, 1.

[14] X. Shu, H. Zheng, G. Xu, J. Zhao, L. Cui, J. Cui, Y. Qin, Y. Wang, Y. Zhang, Y. Wu, *Applied Surface Science* **2017**, *412*, 505.

[15] B. Zhang, V. Cicmancova, J. R. Pereira, J. Kupcik, P. Kutalek, T. Wagner, *Applied Surface Science* **2020**, *530*, 147231.

[16] S. Zhuiykov, Z. Hai, M. K. Akbari, in *2nd International Conference on Battery and Fuel Cell Technology*, **2017**, p. 49.

[17] H. Xie, Z. Li, L. Cheng, A. A. Haidry, J. Tao, Y. Xu, K. Xu, J. Z. Ou, *iScience* **2022**, *25*, 103598.

[18] T. Yang, H. Tian, Y. Zhang, C. Li, *Nano* **2016**, *11*, 1650092.

[19] S. Zhuiykov, Z. Hai, H. Xu, C. Xue, in *World Academy of Science, Engineering and Technology International Journal of Materials and Metallurgical Engineering*, **2017**, pp. 46–49.

[20] Deepika Sandil, S. Srivastava, R. Khatri, K. Sharma, N. K. Puri, *Sens Biosensing Res* **2021**, *32*, 100423.

[21] H. Khan, A. Zavabeti, Y. Wang, C. J. Harrison, B. J. Carey, M. Mohiuddin, A. F. Chrimes, I. A. de Castro, B. Y. Zhang, Y. M. Sabri, S. K. Bhargava, J. Z. Ou, T. Daeneke, S. P. Russo, Y. Li, K. Kalantar-zadeh, *Nanoscale* **2017**, *9*, 19162.

[22] J. Besnardiere, B. Ma, A. Torres-Pardo, G. Wallez, H. Kabbour, J. M. González-Calbet, H. J. von Bardeleben, B. Fleury, V. Buissette, C. Sanchez, T. le Mercier, S. Cassaignon, D. Portehault, *Nature Communications* **2019**, *10*, 327.

[23] S. Zhuiykov, L. Hyde, Z. Hai, M. K. Akbari, E. Kats, C. Detavernier, C. Xue, H. Xu, *Applied Materials Today* **2017**, *6*, 44.

[24] Z. Li, Z. Zhang, Y. K. Kim, R. S. Smith, F. Netzer, B. D. Kay, R. Rousseau, Z. Dohnálek, *The Journal of Physical Chemistry C* **2011**, *115*, 5773.

[25] X. Chen, Y. Zhou, Q. Liu, Z. Li, J. Liu, Z. Zou, *ACS Applied Materials & Interfaces* **2012**, *4*, 3372.

[26] B. Zhang, T. Mikysek, V. Cicmancova, S. Slang, R. Svoboda, P. Kutalek, T. Wagner, *Pure and Applied Chemistry* **2019**, *91*, 1787.

[27] B. Zhang, V. Cicmancova, J. R. Pereira, J. Kupcik, P. Kutalek, T. Wagner, *Applied Surface Science* **2020**, *530*, 147231.

[28] V. I. Shapovalov, A. E. Komlev, A. S. Bondarenko, P. B. Baykov, V. v. Karzin, *Physics Letters A* **2016**, *380*, 882.

[29] R. Suewaka, K. Nakamura, *Japanese Journal of Applied Physics* **2020**, *59*, 015502.

[30] C.-H. Huang, H. Chang, T.-Y. Yang, Y.-C. Wang, Y.-L. Chueh, K. Nomura, *ACS Applied Materials & Interfaces* **2021**, *13*, 52822.

[31] C. W. Ong, H. Y. Wong, G. K. H. Pang, K. Z. Baba-Kishi, C. L. Choy, *Journal of Materials Research* **2001**, *16*, 1541.

[32] L. Pan, Q. Han, Z. Dong, M. Wan, H. Zhu, Y. Li, Y. Mai, *Electrochimica Acta* **2019**, *328*, 135107.

[33] J. McCarthy, T. S. Perova, R. A. Moore, S. Bhattacharya, H. Gamble, B. M. Armstrong, *Scanning* **2006**, *26*, 235.

[34] J. E. Flores-Mena, J. Díaz-Reyes, J. A. Balderas-López, *Revista Mexicana de Fisica* **2012**, *58*, 504.

[35] M. Pham Thi, *Chemical Physics Letters* **1985**, *115*, 130.

[36] H. Sopha, M. Krbal, S. Ng, J. Prikryl, R. Zazpe, F. K. Yam, J. M. Macak, *Applied Materials Today* **2017**, *9*, 104.